J. Fluid Mech. (2013), *vol.* 736, *pp.* 641–662. © Cambridge University Press 2013
doi:10.1017/jfm.2013.552

Spin-up of a magnetically driven tornado-like vortex

Tobias Vogt†, Ilmārs Grants, Sven Eckert and Gunter Gerbeth

Institute of Fluid Dynamics, Helmholtz-Zentrum Dresden-Rossendorf, PO Box 510119, 01314 Dresden, Germany

(Received 5 August 2013; revised 24 September 2013; accepted 10 October 2013; first published online 14 November 2013)

The spin-up of a concentrated vortex in a liquid metal cylinder with a free surface is considered experimentally and numerically. The vortex is driven by two flow-independent magnetic body forces. A continuously applied rotating magnetic field provides the source of the angular momentum. A pulse of about one order of magnitude stronger travelling magnetic field drives a converging flow that temporarily focuses this angular momentum towards the axis of the container. A highly concentrated vortex forms that produces a funnel-shaped surface depression. We explore experimentally the duration, the depth and the conditions of formation of this funnel. Additionally, we measure the axial velocity and calculate the axisymmetric flow field of this transient vortex at a lower force magnitude. The spin-up vortex is similar to the corresponding developed time-averaged turbulent vortex driven by the same magnetic forces (Grants *et al.*, *J. Fluid Mech.*, vol. 616, 2008, pp. 135–152). There are two main differences. First, the maximum swirl concentration condition cannot be expressed as a constant ratio of the two driving forces. Second, a much higher degree of swirl concentration is feasible. We explain these differences as due to a much lower turbulence during the spin-up.

Key words: geophysical and geological flows, rotating flows, vortex dynamics

1. Introduction

A converging flow in combination with a far-field rotation leads to a swirl accumulation towards the convergence zone due to the angular momentum conservation. This phenomenon is also known as vortex stretching and is responsible for a variety of spectacular flows such as tornadoes (see Klemp 1987; Markowski *et al.* 2008; Rotunno 2013) and tropical cyclones (Emanuel 1991, 2003). Because of their destructive nature, there is great interest in understanding this flow phenomenon and, thus, a vast literature is available. However, there are comparatively few laboratory experiments. One of the most important experimental setups is the Ward-type vortex chamber (Ward 1972). This device produces an adjustably convergent airflow through a rotating cylindrical mesh made of fine wires which imposes controlled angular momentum inflow. The flow rate through this vortex chamber is controlled by a variable-speed exhaust fan at the top of the chamber. By this, Ward was able to produce distinct tornado features which were illuminated by smoke tracers. An

† Email address for correspondence: t.vogt@hzdr.de

https://doi.org/10.1017/jfm.2013.552 Published online by Cambridge University Press

advanced version of the Ward-type vortex chamber was reported by Church, Snow & Agee (1977) and Church *et al.* (1979). The main essence of Church's investigations is that the tornado features depend mainly on the swirl ratio of the flow and much more weakly on Reynolds number *Re*, whereby the swirl ratio is defined as the ratio of the flow circulation to the updraft strength. During a stepwise increase of the swirl ratio he observed the following vortex configurations: (i) a single laminar vortex; (ii) a single vortex with breakdown bubble separating the upper turbulent region from the lower laminar region; (iii) a fully developed turbulent core, where the breakdown bubble penetrates to the bottom of the experimental chamber; (iv) vortex transition to two intertwined helical vortices; (v) higher-order multiple-vortex configurations that form in the core region. Numerical simulations following the Ward-type chamber setup are faced with the problem of open boundaries (see references in Rotunno 2013), at which the in- or outlet conditions are poorly defined. In order to overcome this difficulty, Fiedler (1995) introduced an idealized numerical domain for tornado simulations without any in- or outlet boundaries. This closed domain approach was adopted for a number of numerical simulations (Lewellen, Lewellen & Sykes 1997; Fiedler 1998, 2009; Lewellen, Lewellen & Xia 2000; Nolan 2005) for a wide range of swirl ratios and *Re*. These numerical simulations, referred to as the Fiedler chamber, have revealed various features of tornado-like vortices and have confirmed qualitatively their dependence on the swirl ratio.

Probably the closest laboratory analogue of the Fiedler chamber so far is the setup used by Grants *et al.* (2008). In this experiment, a cylindrical container filled with a low-melting-temperature alloy was exposed to a rotating magnetic field (RMF) in order to generate circulation. In addition to the RMF, a vertically travelling magnetic field (TMF) was used to create a converging meridional flow. The advantage of the magnetic fields is the possibility of inducing well-defined flow-independent body forces by contact-less means. Thus, it is possible to construct a closed-flow laboratory analogue of the numerical Fiedler chamber. The ratio of the two magnetic field strengths was varied stepwise, which is an analogy to a variation of the swirl ratio. Swirl accumulation and several similarities to intense atmospheric vortices have been observed, though the developed flow, however strong, did not produce a stable funnel at the free top surface like the one observed in the magnetic bar stirrer flow (Halász *et al.* 2007) or above the drain (Andersen *et al.* 2006). The speculated cause was the intense turbulence that limited the swirl accumulation. Indeed, a transient spin-up flow driven by the same magnetic forces developed a prominent and reproducible, although temporary, funnel-like surface depression (Grants *et al.* 2009). This vortex was able to entrain floating unwetted particles into the bulk.

The aim of the present study is to explore systematically this spin-up vortex. We intend to find the duration, the intensity and the flow patterns, as well as the conditions of the double-cell formation in such a transient flow. Another modification of the setup by Grants *et al.* (2008) is the enlarged container that increases the magnitude of the available body forces and, thus, their effect on the free surface. This allows visual observation of the surface features. Our primarily experimental study is supplemented by a numerical simulation that assumes laminarity and axial symmetry during the spin-up.

Besides the similarity to the intense atmospheric vortices, the considered transient flow may also find a practical application for the purpose of contact-less mixing of floating particles into molten metal, for instance, during the production of oxide dispersion strengthened (ODS) alloys.

https://doi.org/10.1017/jfm.2013.552 Published online by Cambridge University Press

2. Experimental setup

2.1. *Fluid and container*

The experiments were performed in cylindrical containers which were filled with the eutectic alloy GaInSn, that has a melting temperature of $T_0 = 10.5\,^{\circ}\mathrm{C}$. At room temperature, this alloy has a viscosity of $\nu = 3.4 \times 10^{-7}\ \mathrm{m^2\ s^{-1}}$, a density of $\rho = 6.36 \times 10^3\ \mathrm{kg\ m^{-3}}$ and an electrical conductivity of $\sigma = 3.2 \times 10^6\ \mathrm{S\ m^{-1}}$. Two cylindrical Perspex containers were used. The smaller cylinder has a diameter of $D_0 = 2R_0 = 60$ mm and is filled up to a height of $H_0 = 60$ mm with the liquid metal. The larger cylinder has a diameter of $D_0 = 2R_0 = 170$ mm and is filled up to a height of $H_0 = 170$ mm. Hence, the aspect ratio of the liquid metal in both cylinders was $A = H_0/2R_0 = 1$. In order to avoid oxidation, the free surface of the liquid metal is covered in both cylinders with $\sim$1 mm thick layer of hydrochloric acid. Thus, the boundary condition of the upper surface can be regarded as nearly stress-free (or free-slip). The smaller cylinder was used mainly for velocity measurements, while the larger one was used for observation of the free surface deformation and detection of the funnel depth.

2.2. *Measuring technique*

An ultrasound Doppler velocimeter (UDV) (model 2125, Signal Processing SA, Lausanne) was used in the experiments for both the fluid velocity measurements and for the funnel depth detection. In the case of the smaller cylinder, one 8 MHz ultrasound transducer (TR0805LS, acoustic active diameter 5 mm) was attached at the bottom of the container (see figure 1). The transducer measures the vertical velocity distribution in the cylinder along the ultrasound beam which coincides with the container axis. The UDV device records the vertical velocity profiles with a frequency of approximately 10 Hz. The spatial resolution of this measuring technique is determined mainly by the diameter of the ultrasound transducer and by the ultrasound signal settings. In the lateral direction, this resolution is $\sim$5 mm, according to the sensor's active diameter. The lateral resolution slightly increases in the measuring direction due to a divergence of the ultrasound beam of $\sim 3^{\circ}$. The resolution in the axial direction is $\sim$1.4 mm. In the larger cylinder, we have attached a 4 MHz transducer (TR0410SS, acoustic active diameter 10 mm) at the bottom of the container whereby the ultrasound beam again coincides with the container axis. Instead of measuring the axial fluid velocity, we have used some modified settings for the UDV device in order to detect the vertical position of the free surface along the beam line. The main modification was a reduction of the echo detection sensitivity. In this way the echo from microscopic particles was blinded out. Instead, only the position of the strong echo from the free surface was detected and recorded. Additionally, a video camera was mounted above the container in order to synchronously record the free surface shape.

2.3. *Magnetic device*

The experiments were carried out in the magnetic induction system PERM at Helmholz-Zentrum Dresden-Rossendorf (HZDR). The same inductor was used by Grants *et al.* (2008). It is designed for the combined generation of RMF and TMF whereby the field parameters B_R, B_T, ω_R and ω_T can be controlled independently. The RMF is generated by a radial arrangement of six coils, whereby opposing coils are connected as pole-pairs. A three-phase power supply generates an RMF in the centre of the coil arrangement analogous to the stator of an asynchronous motor. The

https://doi.org/10.1017/jfm.2013.552 Published online by Cambridge University Press

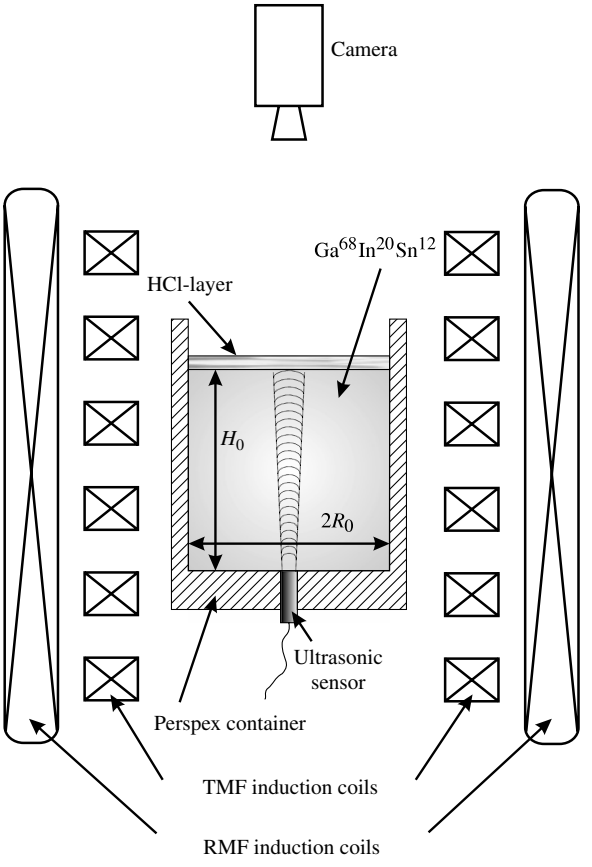


FIGURE 1. Schematic drawing of the experimental setup.

TMF is generated inside a line-up of six coils at an equal distance of $h = 0.048$ m, yielding a wavenumber of $\kappa = 2\pi/(6h) = 21.8$ m^{-1}. The maximum field strength of the inductor for the RMF and TMF is $B_R \approx 17$ mT and $B_T \approx 20$ mT, respectively. The magnetic field strength applied in our experiments is of the order of $B_R \approx 1$ mT and $B_T \approx 10$ mT. The magnetic fields of the PERM device are induced inside a bore hole having the dimensions of $R_b = 200$ mm and $H_b = 300$ mm. The filled cylinders were placed concentrically at the mid-height of this bore hole. In all results presented in this work, the frequency of the RMF is $\omega_R/2\pi = 30$ Hz and the TMF frequency is $\omega_T/2\pi = 60$ Hz. The different frequencies are used to keep the interaction between the RMF and TMF low (Cramer, Pal & Gerbeth 2007).

3. Magnetic body forces

Under the common low-frequency and low-induction conditions the RMF and TMF induce magnetic body forces with a well-known distribution (Grants *et al.* 2008). The RMF induces a purely azimuthal force whose time-averaged value is given by

$$F_\phi = \sigma \omega_R B_R^2 r f(r, z). \tag{3.1}$$

https://doi.org/10.1017/jfm.2013.552 Published online by Cambridge University Press

The force distribution is expressed by the shape function $f(r, z)$ which is maximum at the half-height near the container sidewall. This force drives a rotating flow with secondary meridional circulation (Davidson 1992). The dimensionless force magnitude is given by the magnetic Taylor number

$$Ta = \frac{\sigma \omega_R B_R^2 R_0^4}{\rho \nu^2}. \tag{3.2}$$

The RMF-driven azimuthal flow has been studied experimentally by Robinson & Larsson (1973). No-slip at the horizontal walls drives two recirculation tori in the meridional plane (Davidson 1992), which can be measured by UDV (Räbiger, Eckert & Gerbeth 2010).

The TMF creates an axially directed force whose time-averaged value is given by Grants & Gerbeth (2004) as

$$F_z = \tfrac{1}{4}\sigma \omega_T B_T^2 \kappa r^2. \tag{3.3}$$

Depending on the direction of the TMF wave vector, the liquid metal at the outer part of the container is pushed up- or downwards which drives an axisymmetric flow torus. The dimensionless magnitude of this force is

$$F = \frac{\sigma \omega_T B_T^2 \kappa R_0^5}{2\rho \nu^2}. \tag{3.4}$$

The magnetic flux density of both magnetic fields B_R and B_T in (3.2) and (3.4), respectively, is given in terms of the r.m.s. value.

The magnetic force expressions (3.1) and (3.3) assume a low frequency of the respective alternating magnetic field. This is fulfilled if the shielding factor (Tacke & Schwerdtfeger 1979)

$$S = \mu_0 \sigma \omega R_0^2, \tag{3.5}$$

where μ_0 is the magnetic permeability, is less than 3 (Davidson 1992). For the TMF in the larger container we have $S \approx 11$ which distorts the force distribution considerably, though the effect of S on the velocity distribution remains comparatively low (Lantzsch *et al.* 2007).

4. Experimental results

The experiments were performed as follows. At the beginning of each measurement the flow was set in motion by the RMF alone for ∼600 s in order to achieve a stationary background rotation. This time interval is at least two times the spin-up time (Nikrityuk *et al.* 2005) and ensures that the acceleration of the liquid metal is completed. The spin-up of the tornado-like vortex starts when a much stronger TMF is switched on additionally to the RMF at $t = 0$ s. The ramp-up time of the TMF of ∼1.2 ms was measured by an oscilloscope. The upwards directed TMF created a radially converging flow at the liquid metal surface that resulted in a swirl accumulation towards the convergence zone and the formation of a concentrated vortex. An example of a vortex funnel is shown in figure 2. The snapshot of the free surface represents the flow at $t = 1.8$ s in the large container ($D_0 = 170$ mm) at $Ta = 1.4 \times 10^7$ and $F = 10^{10}$.

The lifetime of such a vortex funnel was limited to only a few seconds owing to the rapidly upcoming turbulence. The whole spin-up process may be divided into three distinct stages. During the first stage ($t < 1$ s) the poloidal flow accelerated and the free surface remained relatively smooth. During the second stage ($1 < t < 2$ s) the

https://doi.org/10.1017/jfm.2013.552 Published online by Cambridge University Press

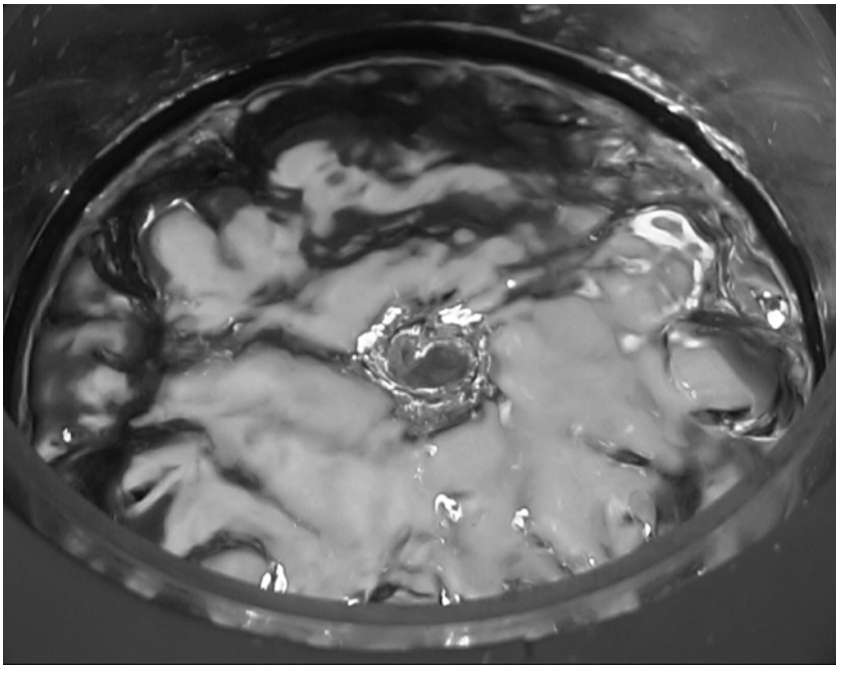


FIGURE 2. Snapshot of the free surface showing the tornado-like vortex funnel in the 170 mm container at $t = 1.8$ s; $Ta = 1.4 \times 10^7$; $F = 1 \times 10^{10}$.

funnel was born at the centre of the top surface and grew in depth while its diameter and location remained nearly unchanged. Figure 3 displays four equispaced snapshots of the free surface as the flow progresses from $t = 0.6$ to 1.2 s. The mirror-like surface was largely axisymmetric during the first stage (figure 3*a*,*b*) and became increasingly wavy during the second stage, figure 3(*c*,*d*). Those waves were arranged around the rim of the surface and their azimuthal periodicity was $m = 12$ in most cases (figure 4). This periodicity corresponds to the number of pieces the inductor's magnetic yoke is made off. During the third stage ($t > 2$ s) the amplitude and the radial extent of the surface waves grew while the funnel typically moved away from the centre in a random direction and finally disappeared. The duration of this final stage was random between 1 and 2 s. In the following subsection we will focus on the second stage.

4.1. *Funnel depth detection*

Earlier investigations have revealed that a tornado-like vortex depends sensitively on the ratio of the flow circulation to the updraft strength, which is expressed by the swirl ratio. The ratio of the two magnetic forces Ta/F is analogous to the swirl ratio in our case. The snapshots in figure 4(*a–e*) display the free surface at $t \approx 1.5$ s for different force ratios $Ta/F = 10, 14, 25, 50$ and $100(\times 10^{-4})$, respectively. These values cover a range of a significant change. The vortex funnel at the low force ratio $Ta/F = 10 \times 10^{-4}$ (figure 4*a*) was thin and apparently deep. The diameter of the funnel grew with the force ratio (figure 4*b*,*c*). At $Ta/F = 50 \times 10^{-4}$ (figure 4*d*) one can observe the transition to two vortices. When the force ratio was further increased ($Ta/F = 100 \times 10^{-4}$), the number of simultaneously occurring vortices and the radius of their circular path increased. This tendency is illustrated by figure 4(*e*), where five

https://doi.org/10.1017/jfm.2013.552 Published online by Cambridge University Press

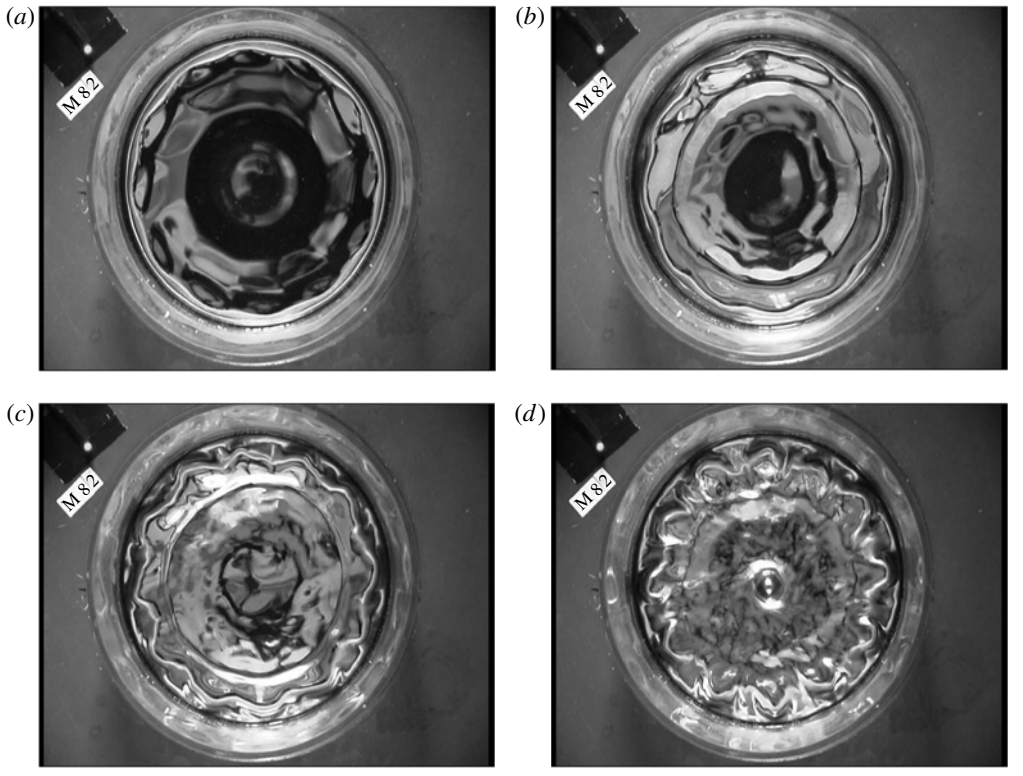


FIGURE 3. Consecutive snapshots of the free surface during the spin-up at $t = 0.6, 0.8, 1.0$ and 1.2 s in (*a–d*), respectively. The TMF strength is $F = 6.6 \times 10^9$ and the relative RMF strength is $Ta/F = 14 \times 10^{-4}$.

vortices are seen. These five vortices remained nearly equidistant and travelled on a circular path around the centre of the container. Video sequences of the free surface corresponding to figure 4 are available as supplementary online material at http://dx.doi.org/10.1017/jfm.2013.552.

Figure 5 shows the variation of the ultrasound echo strength in time along the beam line. Maxima of the echo at the top of these plots mark the position of the macroscopic horizontal reflective surface. A reflective surface below the initial filling level at 170 mm can be either the tip of the funnel or the bottom of smaller cavities this funnel may have spawned. The echo magnitude in figure 5 increases from (*a*) to (*e*) due to increasing funnel radius (cf. figure 4). However, the vertical position of the echo maximum corresponds to the depth of the vortex funnel as long as it persists at the axis of the container and, thus, falls onto the ultrasound beam line. This is ensured during the second stage of the spin-up. The deepest descent of the reflective surface ($\approx$90 mm) was observed at the lowest force ratio of $Ta/F = 10 \times 10^{-4}$ just before the collapse of the funnel at $t = 2.5$ s (figure 5*a*). Note that in this case parts of the echo came from the level of the top surface at 170 mm because, apparently, the beam diameter exceeded the diameter of the funnel base. Multiple echo maxima at the same time instant at $t \approx 1.8$–2.5 s may have been produced by bubbles breaking away from the funnel tip. A single small bubble was seen floating on the free surface after the TMF was switched off. Only a slight increase of the force ratio to $Ta/F = 14 \times 10^{-4}$

https://doi.org/10.1017/jfm.2013.552 Published online by Cambridge University Press

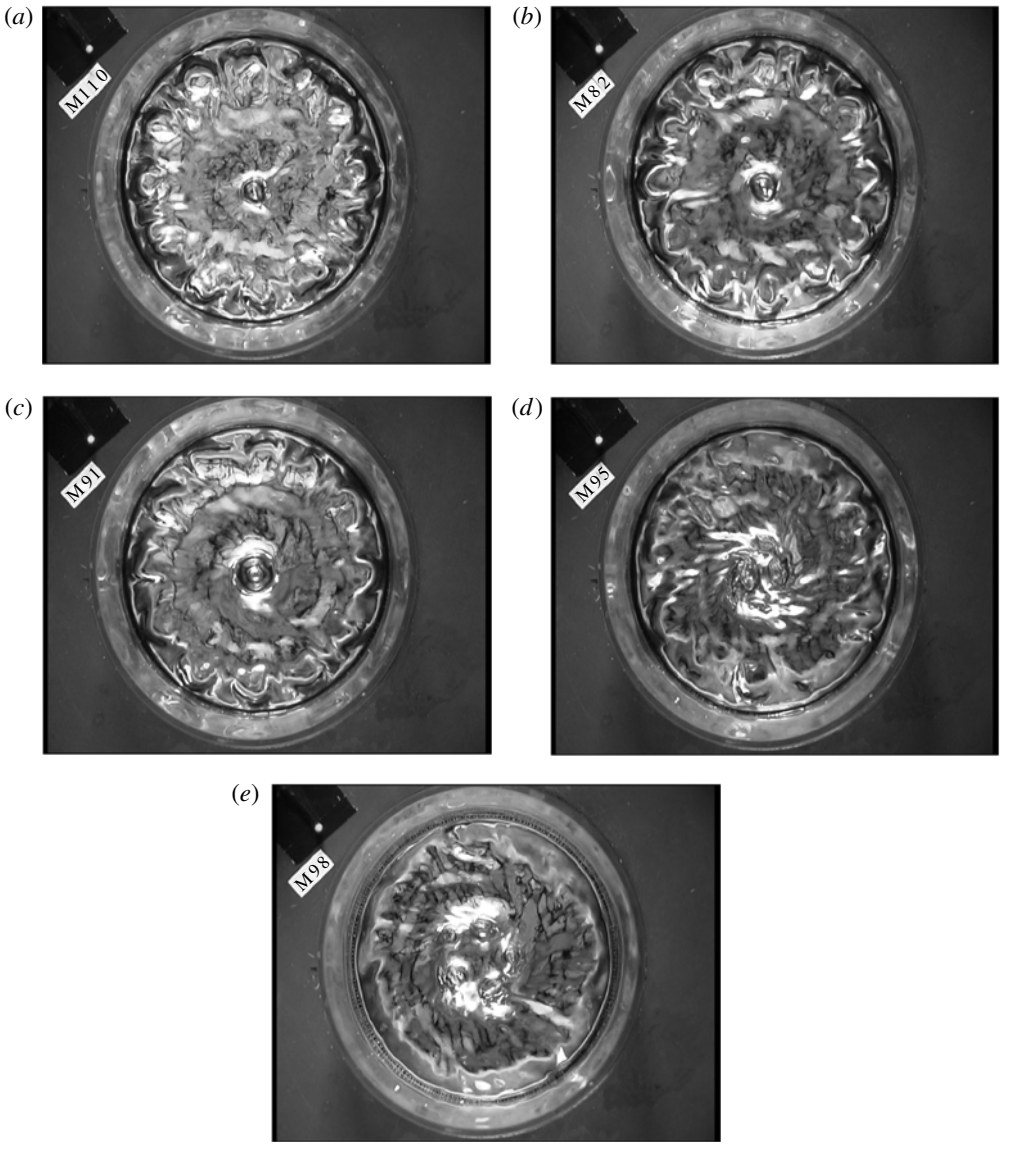


FIGURE 4. Snapshots of the free surface at $t \approx 1.5$ s. The TMF strength is $F = 6.6 \times 10^9$; the relative RMF strength is $Ta/F = 10$, 14, 25, 50 and $100(\times 10^{-4})$for (*a–e*), respectively.

produced a remarkably different echo signature with a single maximum along the beam line for $t = 1.2$–2.5 s (figure 5*b*). This measurement shows an additional surface prominence at $t \approx 4$ s which can be explained as follows. The funnel that formed at $t \approx 1$ s was shifted off the axis at $t \approx 2.5$ s by increasing turbulence and, thus, was no longer visible in the ultrasound beam line. As seen in the synchronous video sequence the funnel has reappeared in the beam line during the third stage of the spin-up at $t \approx 4$ s shortly before collapsing. The more the force ratio was increased the shallower the central depression became (figure 5*c–e*).

https://doi.org/10.1017/jfm.2013.552 Published online by Cambridge University Press

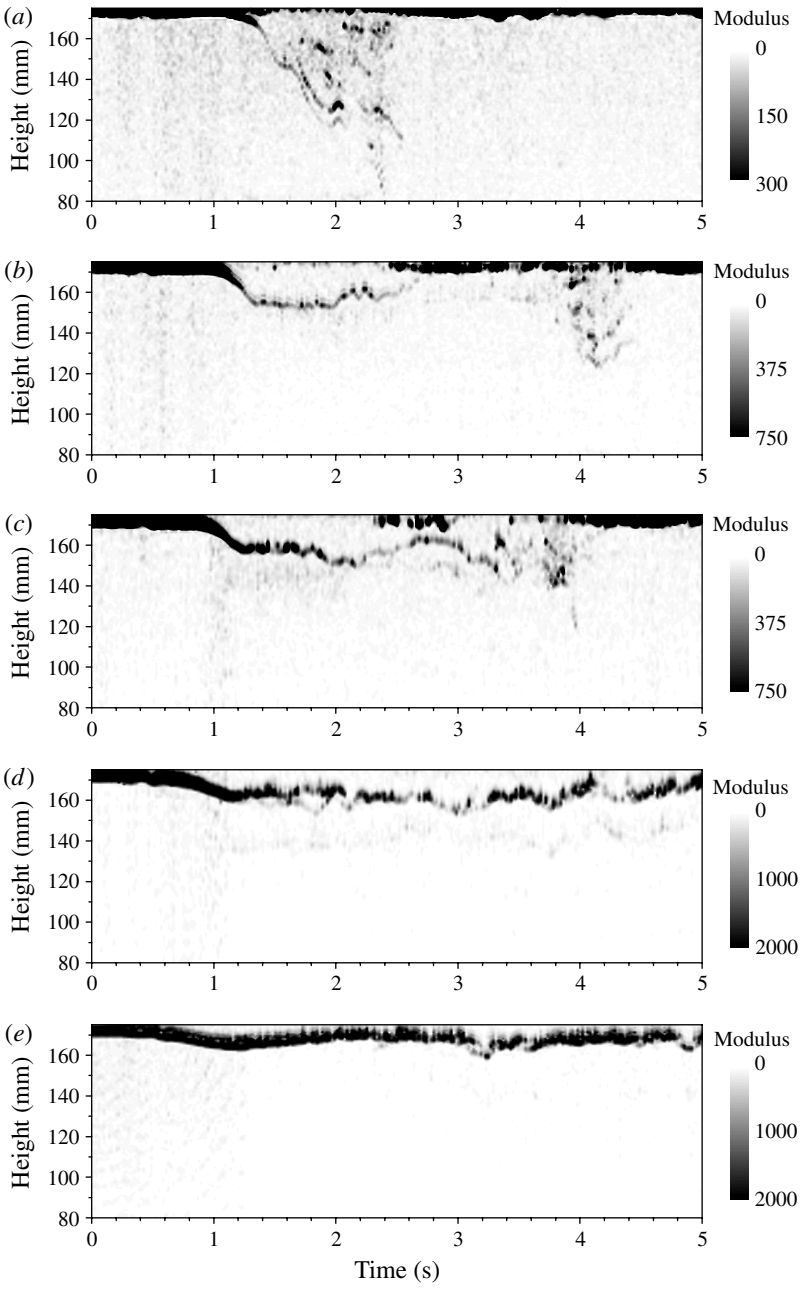


FIGURE 5. Temporal evolution of profiles of the ultrasound echo modulus. A high value reveals position of a reflective surface (bottom of the funnel or a macroscopic bubble) along the beam line. The magnetic field parameters are as in figure 4.

4.2. *Velocity measurements*

The axial velocity measurements are made in the smaller 60 mm container because the reduced cell size results in a much smaller surface deformation and in a longer spin-up. Both effects improve the transient velocity measurement conditions. Figure 6

https://doi.org/10.1017/jfm.2013.552 Published online by Cambridge University Press

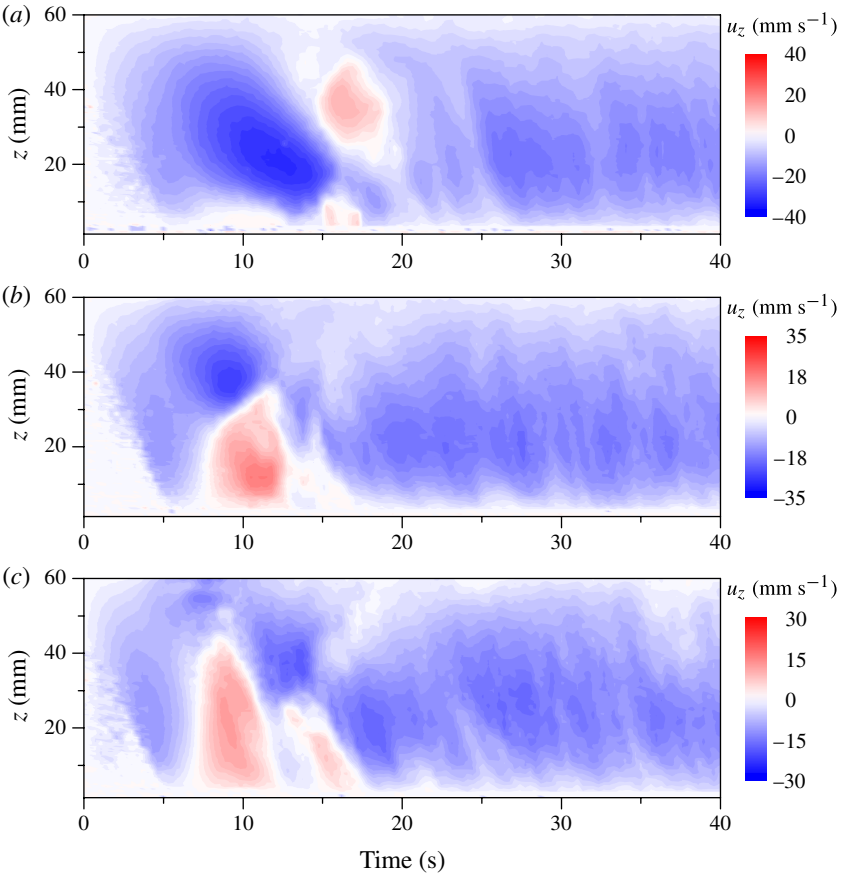


FIGURE 6. Spatio-temporal evolution of the ensemble-averaged axial velocity along the axis at different force ratios: (*a*) $Ta/F = 0.0037$; (*b*) $Ta/F = 0.0072$ and (*c*) $Ta/F = 0.0112$. $D_0 = H_0 = 60$ mm; $F = 4.8 \times 10^6$.

shows the evolution of the ensemble-averaged vertical velocity profiles along the axis from five repeated measurements. In this figure, a positive value of u_z describes an upwards directed flow, negative values a downward one. The force ratio was increased from $Ta/F = 0.0037$ to 0.0112 whereby the upwards directed forcing $F = 4.8 \times 10^6$ was kept constant. The flow prior the measurements was again set in a stationary rotating motion by RMF alone and then the TMF is switched on at $t = 0$ s. As we shall see later (§ 6), the transition between different flow patterns cannot be attributed to the force ratio alone. There is also a dependence on the absolute value of F. The results showed that the transition occurred at a higher Ta/F than in the larger container (figures 4 and 5). Figure 6(*a*) shows the axial velocity at a weak RMF ($Ta/F = 0.0037$) that did not significantly alter the TMF-alone-driven flow. The maximum speed of this downwards directed flow was reached at $t \approx 13$ s and $z/H_0 \approx 1/3$. A weak flow reversal was afterwards observed in the upper half of the container. At $t \approx 25$ s the flow reached a steady state with a downwards directed axial velocity along the container axis. Figure 6(*b*) displays the axial flow at an intermediate force ratio. The downwards directed flow speed during the initial adjustment phase was much lower. At $t \approx 6$ s a region emerged with upwards directed

https://doi.org/10.1017/jfm.2013.552 Published online by Cambridge University Press

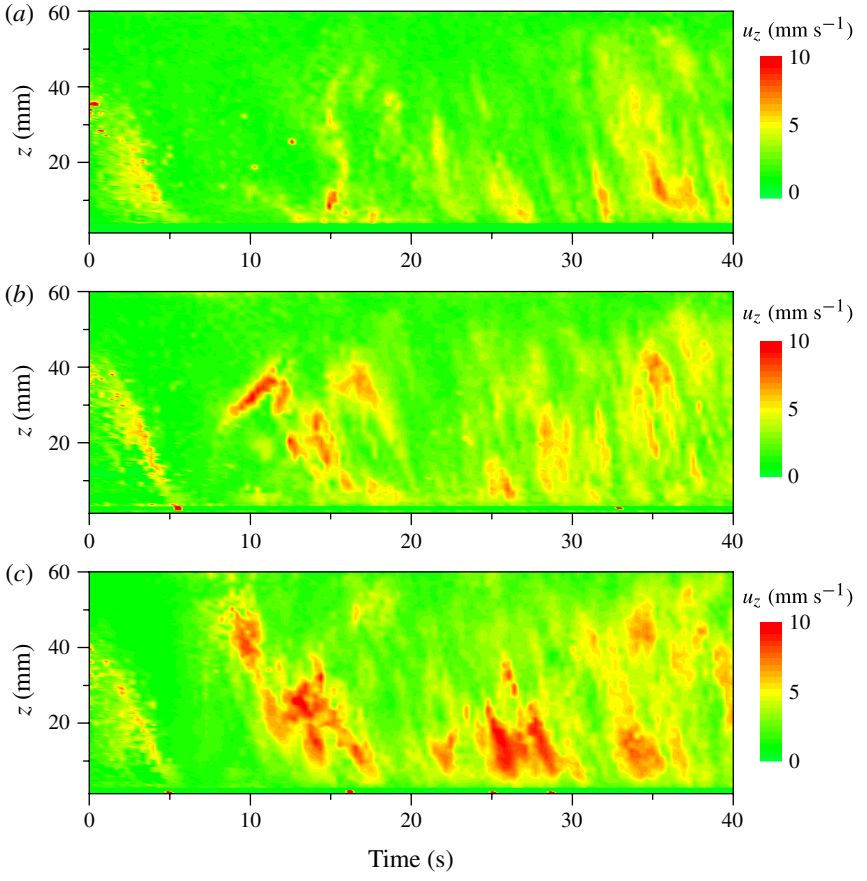


FIGURE 7. Spatio-temporal evolution of the standard deviation of the axial velocity at different force ratios: (*a*) $Ta/F = 0.0037$; (*b*) $Ta/F = 0.0072$ and (*c*) $Ta/F = 0.0112$. $D_0 = H_0 = 60$ mm; $F = 4.8 \times 10^6$.

flow. This region quickly spread to about half of the container height. The maximum speed of the upward flow was reached at $t \approx 12$ s. The axial velocity profile did not change significantly during the initial 6 s (figure 6*c*) when the force ratio was further increased. Afterwards, however, the upwards directed flow region expanded to the top surface at $t \approx 10$ s.

Independently of the RMF strength the transient axial velocity profiles appeared reproducible during the initial spin-up. That was followed by increasing randomness due to onset of turbulence at a later stage. In order to estimate the instant of the turbulence onset we have calculated the transient standard deviation of individual measurements (figure 7) from their ensemble-average profiles shown in figure 6. Each standard-deviation plot in this figure was calculated from five measurements. In all three cases displayed in figure 7 the loss of repeatability occurred at about $t = 8$–15 s, whereby the standard deviation generally increases with increasing Ta/F. Some congruent downward trending peaks were observed from $t = 0$ to 5 s. We suspect that those peaks are artefacts connected to low fluid velocities (cf. figure 6) at the beginning of the measurements.

https://doi.org/10.1017/jfm.2013.552 Published online by Cambridge University Press

5. Numerical techniques

The numerical simulation provides a much wider access to flow variables at a cost of uncertainty due to the model simplifications. Our numerical model is built upon two major assumptions:

(i) the vortex stays axially symmetric during initial laminar spin-up phase;

(ii) the effect of the surface deformation on the velocity field may be neglected.

We consider a transient axisymmetric liquid metal flow in a regular cylinder driven by magnetic forces (3.1) and (3.3). The flow may be described by the following dimensionless equations in stream function and vorticity formulation (Grants & Gerbeth 2001):

$$\frac{\partial \Omega}{\partial t} + \mathscr{N}(\Omega) - \frac{\partial H}{\partial z}\Omega = \mathscr{L}(\Omega) + Taf(r,z), \tag{5.1}$$

$$\frac{\partial W}{\partial t} + \mathscr{N}(W) - \frac{\partial \Omega^2}{\partial z} = \mathscr{L}(W) - F, \tag{5.2}$$

$$\mathscr{L}(H) + 2W = 0, \tag{5.3}$$

where operators $\mathscr{L}$ and $\mathscr{N}$ are expressed as

$$\mathscr{L} = \frac{\partial^2}{\partial r^2} + \frac{3}{r}\frac{\partial}{\partial r} + \frac{\partial^2}{\partial z^2}, \quad \mathscr{N} = \left(H + \frac{r}{2}\frac{\partial H}{\partial r}\right)\frac{\partial}{\partial z} - \frac{r}{2}\frac{\partial H}{\partial z}\frac{\partial}{\partial r}. \tag{5.4}$$

The flow velocities can be expressed in terms of the reduced stream function H and the angular velocity Ω as

$$v_z = H + 0.5r\frac{\partial H}{\partial r}, \quad v_r = -0.5r\frac{\partial H}{\partial z}, \quad v_\phi = r\Omega. \tag{5.5}$$

Function $W = r^{-1}(\partial v_r/\partial z - \partial v_z/\partial r)$ represents the azimuthal vorticity. The radius of the cylinder R_0 and the respective momentum diffusion time R_0^2/ν are used as length and time scales in (5.1)–(5.3). The aspect ratio is kept constant at $H_0/2R_0 = 1$ as in the experiment. The boundary conditions are set to free-slip at the top surface

$$W|_{z=1} = 0, \quad H|_{z=1} = 0, \quad \left.\frac{\partial \Omega}{\partial z}\right|_{z=1} = 0, \tag{5.6}$$

and no-slip elsewhere

$$\left.\frac{\partial H}{\partial z}\right|_{z=-1} = 0, \quad H|_{z=-1} = 0, \quad \Omega|_{z=-1} = 0, \tag{5.7}$$

$$\left.\frac{\partial H}{\partial r}\right|_{r=1} = 0, \quad H|_{r=1} = 0, \quad \Omega|_{r=1} = 0. \tag{5.8}$$

The spin-up is observed for constantly applied RMF during a pulse of a comparatively strong TMF. The stationary solution of (5.1)–(5.3) with $F = 0$ is, therefore, used as the initial condition.

5.1. *Solution method*

Equations (5.1)–(5.3) are solved by implicit time-discretization of second-order. The resulting Helmholtz-type equations are solved expressing the solution in series of Chebyshev polynomials and requiring the residual to be orthogonal to the leading

https://doi.org/10.1017/jfm.2013.552 Published online by Cambridge University Press

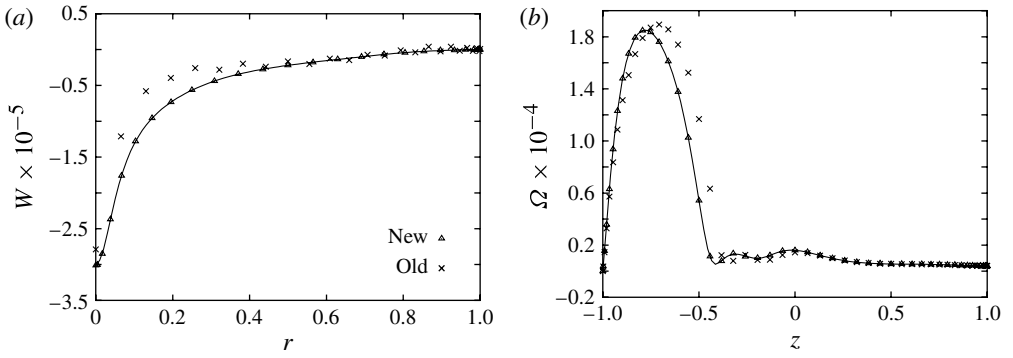


FIGURE 8. Results of the numerical test case with $F = 4 \times 10^5$, $Ta = 2 \times 10^4$ at time instant $t = 0.01114$. The vorticity along the bottom ($z = -1$) and the angular velocity at the axis ($r = 0$) is shown in (*a*) and (*b*), respectively. The high-resolution (109×97 modes) reference solution by the old code (Grants & Gerbeth 2001) is displayed with a solid line. Triangles and crosses display low-resolution (49×25) results with the new and old code, respectively. Note clustering of triangles near $r = 0$ in (*a*) due to transformation (5.9).

expansion terms. The numerical solution is constructed in the same way as in Grants & Gerbeth (2001) with the main differences outlined below.

In contrast to the RMF-alone-driven flow, a sharp variation of flow is expected near the axis. To increase spatial resolution there the following coordinate transformation is used (see §3.4.1 in Canuto *et al.* 1988):

$$x = 2r - 1, \quad r = 0.5(x + 1), \tag{5.9}$$

which maps the $[0 : 1]$ domain of r onto a $[-1 : 1]$ domain of x. Roots of higher-order Chebyshev polynomials tend to cluster near $x = \pm 1$ producing elevated resolution at $r = 0$.

The different boundary conditions at the two horizontal boundaries $z = \pm 1$ break the vertical symmetry of the solution as well as coupling even and odd vertical modes. At the same time the free-slip condition imposes an explicit boundary condition for the function W (5.6). This results in a single spectral dependence matrix encompassing even and odd modes. This matrix links the normal derivative of the stream function H with vorticity along the bottom and sidewalls.

The spatial resolution is increased from $N_r \times N_z = 65 \times 97$ to 97×129 to 145×193 modes as the poloidal forcing varies from $F = 10^6$ to 10^7 to 10^8.

5.2. *Test*

The code with the enhanced resolution at the axis (5.9) was tested using our previous code (Grants & Gerbeth 2001) as a benchmark. To do so, this old code was first modified to satisfy the free-slip conditions (5.6) at the top of the cylinder. Figure 8 shows results of the test for a case with moderate values of F and Ta. It is observed that a much lower number of radial modes is sufficient to resolve the concentrated vortex in the centre of the cylinder with use of (5.9).

6. Numerical results

Let us first consider the dependence $\tau(F)$, where τ is the non-dimensional instant of the first maximum in the axial velocity on the axis at $Ta = 0$. This initial adjustment

https://doi.org/10.1017/jfm.2013.552 Published online by Cambridge University Press

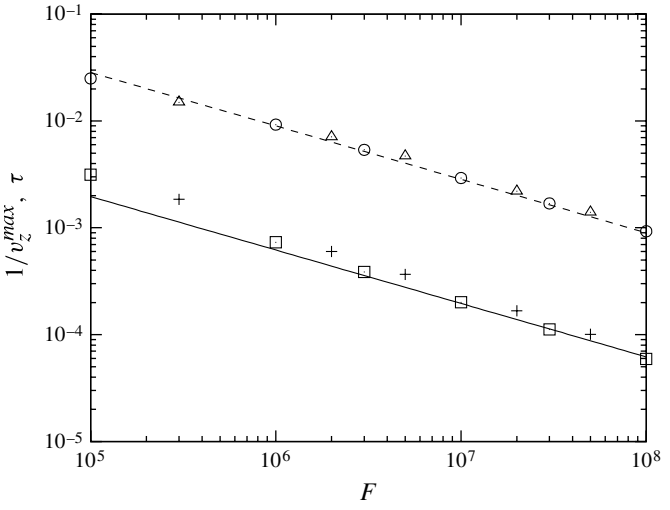


FIGURE 9. The calculated initial adjustment time (circles) and inverse of the maximum axial velocity attained along the centreline (squares) versus F at no rotation. Lines correspond to $O(F^{-1/2})$ scaling. The respective experimental results are displayed by triangles and crosses.

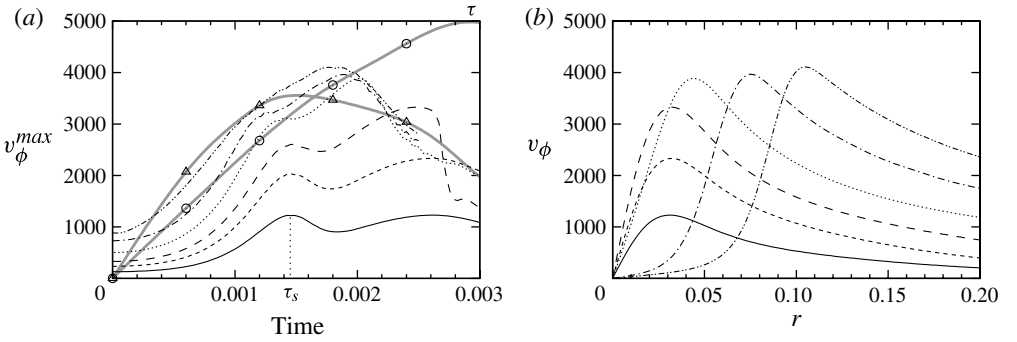


FIGURE 10. Azimuthal velocity on the free surface for $F = 10^7$ and variable Ta: (a) the time dependence of the maximum value; (b) the radial distribution at the instant of the global maximum. Solid, dashed, long-dashed, dotted, dash-dotted and dash-double-dotted lines correspond to $Ta = 1, 2, 3, 5, 8$ and $12(\times 10^4)$, respectively. The thick grey lines in (a) display the maximum axial velocity (circles) and the surface strain rate ($-\partial v_r/\partial r$, triangles) at the axis for $Ta = 0$.

time scaled with the TMF strength as $\propto F^{-1/2}$ while the maximum axial velocity scaled as $\propto F^{1/2}$ (figure 9).

Provided that Ta is sufficiently small the azimuthal velocity field should act like a passive scalar. In that case the spin-up duration is determined solely by the TMF. Figure 10 shows the transition from such a passive spin-up to a regime with a strong swirl feedback as Ta was increased at a constant $F = 10^7$. The first maximum of the swirl was observed (figure 10a) at $t = \tau_s \approx \tau/2$ ($\tau = 0.00292$ for $F = 10^7$). Figure 11 shows the development of the surface angular momentum $\Gamma(r) = r^2\Omega(r, 1)$ and radial velocity profiles for $t < \tau_s$. The location of the maximum angular momentum initially

https://doi.org/10.1017/jfm.2013.552 Published online by Cambridge University Press

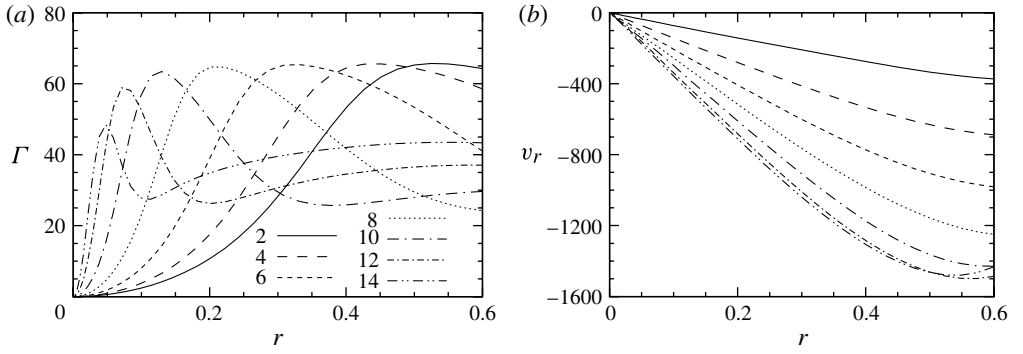


FIGURE 11. Consecutive snapshots of (*a*) the angular momentum and (*b*) the radial velocity profiles during the spin-up for $F = 10^7$ and $Ta = 10^4$. Numbers in the legend correspond to the dimensionless time in units of 10^{-4} (cf. figure 10*a*).

moved inwards with nearly constant speed for $t \leqslant 10^{-3}$. Later at $t \approx \tau_s$ this movement stalled at some distance from the axis at about the same time as the maximum of the radial velocity was reached (figure 11). The ultimate swirl width r_s, defined as the radial position of the surface azimuthal velocity maximum, was independent of RMF for small enough Ta and increased with Ta once a certain threshold of RMF strength Ta_{tr} was reached (figures 10*b*, 12*a*). As the swirl width increased beyond Ta_{tr}, the peak azimuthal velocity stayed approximately constant slightly below the peak axial velocity in the $Ta = 0$ case. The critical force ratio Ta_{tr}/F decreased with F (figure 12*b*), less so with a solid cover at the top surface. The radius of the vortex near the transition decreased with F (figure 12*c*).

Figure 13 reveals that significant changes of the axial velocity distribution took place along the centreline for $Ta \approx Ta_{tr}$ at $t > \tau_s$. These changes are further detailed in figure 14. At $t \approx \tau_s$ a vortex breakdown bubble was apparently born at the bottom of the cylinder. For $Ta < Ta_{tr}$ this bubble stayed in the lower part (figure 13*b*,*c*). Otherwise, it rapidly rose, touching the top surface within the initial adjustment time (figure 13*d*).

7. Discussion

We have studied the spin-up of a magnetically driven tornado-like vortex in different dimensionless parameter ranges and by different methods. In this section we will discuss our observations with a focus on the duration, the width, the structure and the funnel depth of this vortex.

7.1. *Spin-up duration and turbulence onset*

The division of the funnel life-cycle into three stages may be based on instants τ_s and τ, when the first maximum of the swirl and of the axial velocity, respectively, is reached, the latter followed a scaling $\tau = O(F^{-1/2})$ confirmed both experimentally and numerically (figure 9). Extrapolation of numerical results in figure 9 to the conditions in figures 4 and 5 produces $\tau = 1.1 \times 10^{-4}$ or 2.3 s in dimensional terms. This matches the duration of the two first deterministic stages of the funnel life-cycle almost perfectly (see figure 5*a–c*). This scaling may be discussed as follows. Initially the inertia of almost motionless liquid (the $\partial v_z/\partial t$ term) balances most of the TMF-induced axial force $O(F)$. The acceleration ends when the material derivative

https://doi.org/10.1017/jfm.2013.552 Published online by Cambridge University Press

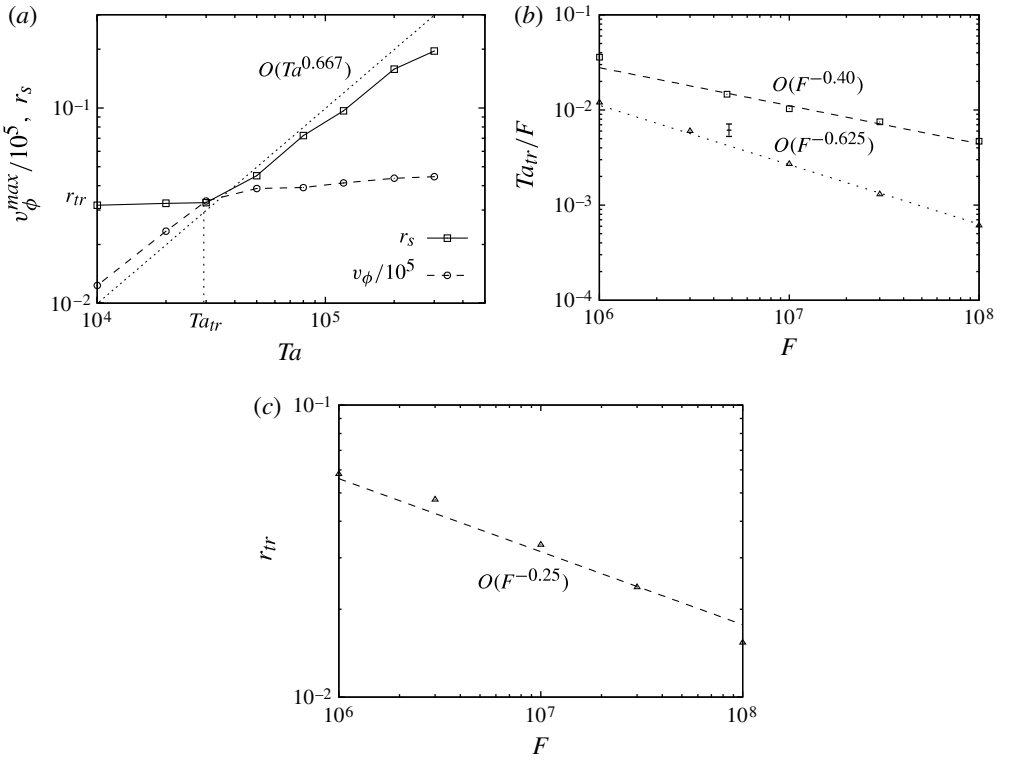


FIGURE 12. Transition from a passive to a 'strong' swirl. (*a*) Dependence of the maximum attained surface azimuthal velocity and the respective vortex radius on RMF intensity near the transition for $F = 10^7$ (cf. figure 10*b*). (*b*) The critical force ratio versus F; triangles and squares correspond to free and no-slip top surface boundary conditions, respectively. The experimentally observed transition is displayed by an error bar. (*c*) Dependence of the critical vortex radius on the TMF strength.

term $(v_z \partial v_z/\partial z)$ takes over. The above statements may be expressed as

$$O\left(\frac{v_{max}}{\tau}\right) = O(v_{max}^2) = F. \tag{7.1}$$

From this expression it follows that $v_{max} = O(F^{1/2})$ and $\tau = O(v_{max}^{-1}) = O(F^{-1/2})$.

The time of the funnel onset at $t = 1.2$ s in the experiment (figure 5*a–c*) correlated with the numerically observed first maximum in the surface swirl at $\tau_s \approx 0.5\tau$ (figure 10) although F differed by a factor of 10^3. Apparently, the ratio τ_s/τ was invariant with F. This invariance may be discussed as follows. The swirl reached its first maximum when the inward transport of the angular momentum stalled at $r \approx r_s$ (figure 11*a*). Let r_0 be the initial location of the angular momentum maximum. The distance $r_0 - r_s$ this maximum travelled inwards changed very little with F, because r_0 depends only on Ta but $r_s \ll r_0$. If the characteristic velocity of this movement scales as v_z^{max}, then it increases with F by the same amount as the spin-up time τ decreases (figure 9). Thus, τ_s/τ stayed nearly constant with respect to F.

The duration of the third stage of the funnel life-cycle was random as was the trajectory of its movement for $t > \tau$. This points to turbulence as the cause of the funnel collapse. Quantification of turbulence is complicated by unsteadiness of the

https://doi.org/10.1017/jfm.2013.552 Published online by Cambridge University Press

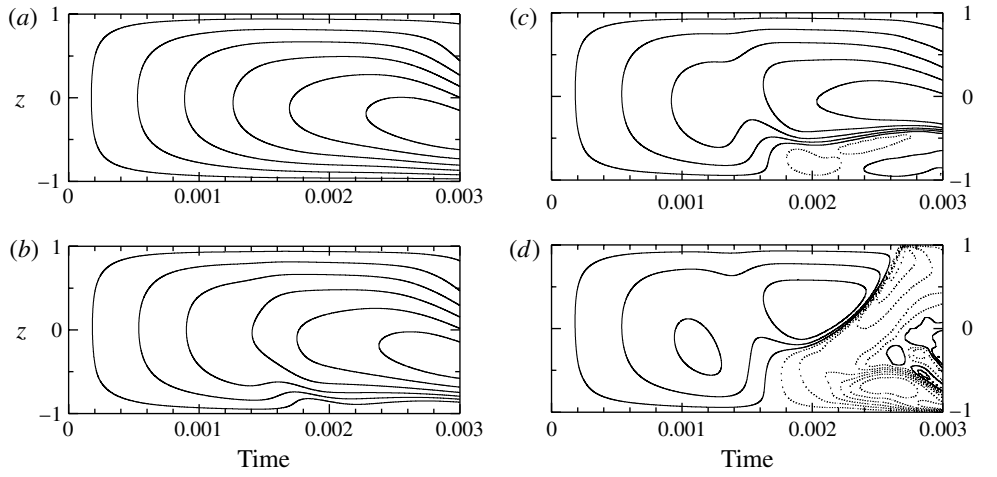


FIGURE 13. The spatio-temporal diagrams of the axial velocity along the axis for $F = 10^7$ and variable $Ta = 0, 1, 2, 3 \times 10^4$ in (*a–d*), respectively. The isoline step is 400. The solid and dotted lines correspond to negative and positive values, respectively.

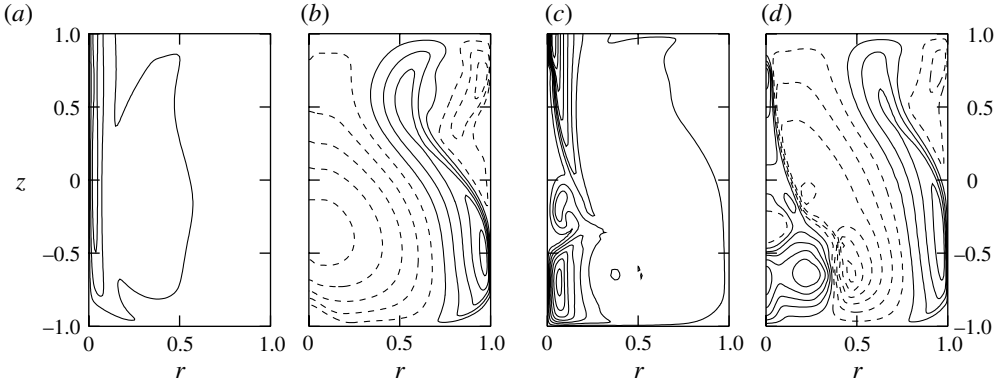


FIGURE 14. Iso-velocity lines of (*a*,*c*) the azimuthal and (*b*,*d*) the axial velocity for $F = 10^7$ and (*a*,*b*) $Ta = 10^4$ at $t = \tau = 0.00292$ or (*c*,*d*) $Ta = 3 \times 10^4$ just before the 'touchdown' of the vortex breakdown at $t = 0.00263$ (cf. figure 13*d*). Isoline step is 400 or 1000 for the azimuthal or axial velocity, respectively. Negative values are depicted with dashed lines.

base flow, which cannot be recovered by time-averaging. An attempt to overcome this difficulty is presented in figures 6 and 7. The base flow is recovered here as the ensemble-average of five repeated measurements. The turbulence, in turn, manifests itself as a deviation from the base flow (figure 7). The velocity profiles remained largely reproducible during the first two stages of spin-up for $t < \tau$, though figure 7 reveals two zones of elevated standard deviation for $t < \tau \approx 13$ s. The first one ($t < 5$ s) was observed in the lower part of the container for any non-zero RMF strength. We suspect that this was an artefact caused by too low velocity values (cf. figure 6). The second zone of an elevated standard deviation was only observed at a sufficiently strong RMF (figure 7*b*,*c*) for $t = 8$–13 s. It coincided with the location of the supposed vortex breakdown, where the sign of the axial velocity changed. We speculate that those standard deviation peaks were caused by a sensitive

https://doi.org/10.1017/jfm.2013.552 Published online by Cambridge University Press

dependence of the transient vortex breakdown position on small random variations of the experimental conditions. Alternatively, the vortex breakdown may have caused a local spot of turbulence. A persistent randomness extending over the whole height occurred after $t = 35$ s or $t \approx 3\tau$. This compares to the maximum funnel lifetime $t \approx 2\tau$ in the larger container. Qualitative evidence of gradual growth of turbulence during the spin-up can also be observed on the surface of the larger container (figure 3). The central part of the surface remained axisymmetric and mirror-smooth during the first stage at $t < \tau_s \approx 1$ s. Apparently, there was very little turbulence. A small-scale waviness arose on the central part of the surface during the second stage (figure 3*c*,*d*) suggesting some more turbulence. Its intensity, however, was insufficient to displace the central vortex from the container axis or to influence the spin-up duration. Note that the spin-up duration agreed reasonably well with the numerical (laminar) scaling extrapolated over two orders of magnitude. The third stage of the funnel life-cycle was essentially random with turbulence, evidently, being source of this randomness.

7.2. *Vortex width*

The vortex width may be discussed with reference to the Burgers vortex (Prochazka & Pullin 1995)

$$v_\phi(r) = \frac{\Gamma_0}{r}(1 - \mathrm{e}^{-\gamma r^2/4}), \tag{7.2}$$

where $\gamma = \partial v_z/\partial z$ is a given constant dimensionless strain rate and Γ_0 is the angular momentum at infinity. This is a steady solution of the Navier–Stokes equation formed by the balance between the convective and the diffusive transfer of angular momentum. In our case the strain rate is transient with the peak value $\gamma_{max} = O(F^{1/2})$ and the ramp-up time $O(F^{-1/2})$. The latter is comparable to the internal time scale of the Burgers solution γ^{-1}. Therefore, the stationary solution (7.2) should still give a correct estimate of the spin-up vortex width. Equation (7.2) implies the characteristic vortex width $r_s = O(\gamma^{-1/2}) = O(F^{-1/4})$ which correlates well to the observed scaling in figure 12(*c*). The straight line in this figure corresponds to the Burgers vortex width evaluated as the radius of the $v_\phi(r)$ maximum from expression (7.2) with $\gamma = v_z^{max} \approx 1.6F^{1/2}$ estimated from figure 9.

The Burgers vortex solution assumes negligible feedback of the swirl to the applied strain rate (i.e. a 'passive swirl'). At some critical circulation, however, the centrifugal force should reach the magnitude of the radial pressure gradient that drives this strain

$$\frac{v_\phi^2}{r} \approx \frac{\partial p}{\partial r}. \tag{7.3}$$

Let us estimate the radial pressure drop as $\Delta p = O(F)$. From (7.3) we then have $v_\phi^{max} = O(F^{1/2})$, as is well-known for the atmospheric vortices (Rotunno 2013) and also observed in our numerical simulation. On the one hand, the conservation of the angular momentum in an inviscid converging flow leads to a $v_\phi = \Gamma_0/r$ profile in the outer part of the vortex. On the other hand, the maximum azimuthal velocity is limited by the centrifugal force to $O(F^{1/2})$

$$\Gamma_0/r_s = O(F^{1/2}) \tag{7.4}$$

which stops the swirl accumulation at a certain distance r_s from the axis. At the transition this distance $r_s = r_{tr}$ approximates the Burgers vortex radius $O(F^{-1/4})$. Inserting the initial angular momentum $\Gamma_0 = O(Ta^{2/3})$ (Davidson 1992) and the

https://doi.org/10.1017/jfm.2013.552 Published online by Cambridge University Press

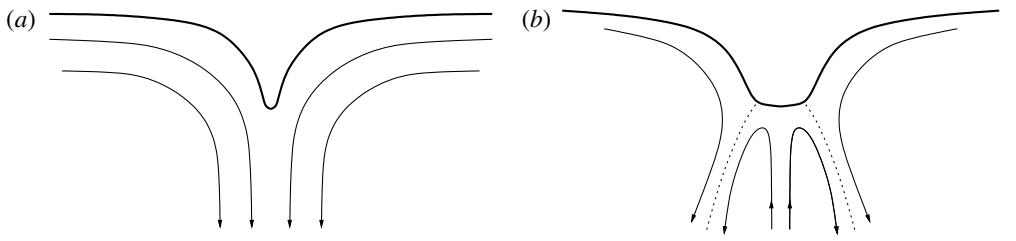


FIGURE 15. Meridional flow topology below the central depression in the case of (*a*) a single-cell and (*b*) a double-cell vortex.

Burgers vortex width $r_s = O(F^{-1/4})$ into (7.4) produces the critical $Ta_{tr} = O(F^{3/8})$, which corresponds to

$$Ta_{tr}/F = O(F^{-5/8}) \tag{7.5}$$

observed in figure 12(*b*). It is easy to see that the above description is also consistent with the '2/3' scaling of $v_\phi^{max}(Ta)$ observed for $Ta < Ta_{tr}$ and $r_s(Ta)$ for $Ta > Ta_{tr}$ (figure 12*a*).

7.3. *Vortex structure*

At a certain swirl ratio the transition to a double-cell-structure vortex is observed in the Ward chamber. In our experiment, this transition would reverse the axial velocity along the vortex axis (see figure 15). Such reversal occurred in our numerical simulation simultaneously with the transition from the fixed-width to the fixed-intensity vortex. The same is also observed experimentally in the related time-averaged turbulent flow (Grants *et al.* 2008) with the difference that the transition occurs at a constant force ratio, $Ta_{tr}/F = \text{const}$, instead of (7.5). Assuming $\Gamma_0 = O(Ta^{1/2})$ dependence in the turbulent flow (figure 5*a* in Grants *et al.* 2008; Robinson & Larsson 1973) and inserting this in (7.4) we obtain $r_{tr} = O(1)$ which is consistent with the experimental observations. The swirl accumulation is, thus, limited to a certain fraction of the container that does not change with F. It may be interpreted as the eddy viscosity growing proportionally to the imposed strain rate in the developed turbulent flow.

We observed the vortex structure change by measuring the axial velocity along the axis in the smaller container. For $F = 4.8 \times 10^6$ it occurred at $Ta/F \in [0.0055 : 0.0075]$ (figure 6). That compares to $\sim$0.0042 in the numerical simulations (figure 12*b*). The difference is probably caused by deviation of the surface conditions from the perfect free-slip. As seen in figure 12(*b*) the surface boundary conditions have a strong impact on the critical force ratio. Alternatively, the difference may be due to turbulence neglected in the numerics.

Reliable instant velocity measurements were not possible in the large container under conditions of the funnel formation, though the underlying vortex structure may be judged from the fact that the vortex diameter shrank as the angular momentum supply was reduced under TMF of a fixed strength (figure 4*a–c*). Such behaviour is not compatible with the 'passive' Burgers vortex. Its diameter based on the molecular viscosity is only $\sim$0.5 mm. We obtained no evidence that the vortex could be focused to such a degree in our setup. Very likely, there was some turbulence and, thus, some eddy viscosity during the spin-up that would limit the swirl accumulation to some larger diameter. Nevertheless, the evidence in figure 4 suggests that this limit

https://doi.org/10.1017/jfm.2013.552 Published online by Cambridge University Press

was not reached at the vortex diameter ≈10 mm and, consequently, a double-cell structure (such as in figure 15*b*) was present in all displayed cases. Such a flow structure with intense opposite vertical streams sharing a narrow space appears very counter-intuitive. Our interpretation is as follows. The double-cell vortex stems from the centrifugal force terminating the radial inflow of the angular momentum at some distance r_s that exceeds the Burgers vortex radius. Being unable to penetrate closer to the axis, the angular-momentum-rich fluid parcels descend at $r \approx r_s$. The resulting intense cyclostrophic 'eyewall' (upper part of figure 14*c*,*d*) imposes certain 'boundary conditions' for the flow within it. Those 'boundary conditions' drive the secondary inner meridional recirculation cell with the reversed axial velocity on the axis. If, on the contrary, the angular momentum inflow is terminated by the molecular or eddy viscosity, then the primary radial flow may penetrate to the axis and a single-cell fixed-diameter vortex forms. In the latter case the swirl is 'passive' and it does not reach its full potential strength. The minimum possible diameter of the double-cell vortex, thus, depends principally on the effective eddy viscosity within the vortex core as well as the strain rate and not directly on the updraft diameter. The presence of solid lateral walls that form the Ward vortex chamber may contribute to the turbulence production and, consequently, to the eddy viscosity in the vortex core. The transient inertial forces during spin-up of a real tornado, in turn, may reduce this eddy viscosity just as happened in our setup. We, therefore, speculate that the natural tornado may form a more slender double-cell vortex (compared to the updraft diameter) than observed in the Ward chamber. The funnel cloud, however thin or distorted (such as, for instance, in figures 2 and 4 in Yih 2007), could be the inner vortex cell with downdraft along the centreline dragging down mist from the parent cloud.

Note that evidence of a slender double-cell vortex has been observed in a magnetic bar stirrer flow. Dye was injected in the vortex centre and a long-lived elongated dye curtain emerging from the middle of the funnel was observed (Halász *et al.* 2007). Without the double cell the dye would disperse into the bulk in a few seconds, just as happens when it is injected outside the core.

7.4. *Funnel depth*

Formation of a deep sharp funnel may be crucial if the spin-up vortex is applied with the purpose of stirring floating unwetted particles into molten metal by contact-less means. A concentrated vortex alone might be insufficient for such a purpose. Evidence in figure 5 suggests that a narrow and deep funnel would produce particle-filled cavities either by the tip instability (Andersen *et al.* 2006) or by funnel collapse at the end of the spin-up. Those cavities would be further split and entrained by the subsequent intense turbulent downdraft.

A reproducible funnel formed at the free surface in the large container with $F > 3 \times 10^9$. The value of the forcing parameter F, however, cannot be a criterion for the funnel formation since F does not account for the restoring properties of the surface. Let us consider, instead, a dimensionless criterion

$$\mathscr{F} = \frac{\sigma \omega_T B_T^2 R_0^2}{2(\rho g s)^{1/2}} \kappa R_0, \tag{7.6}$$

which expresses the ratio of the characteristic dynamic pressure $\rho(\nu/R_0)^2 F$ to the characteristic hydraulic head $\rho g h_c$ of the capillary-force-balanced depression, where $h_c = (s/\rho g)^{1/2}$ is the capillary length and s is the surface tension. From Lundgren's equation for the surface deformation (Andersen *et al.* 2006, equation (5.7))

https://doi.org/10.1017/jfm.2013.552 Published online by Cambridge University Press

it becomes evident that an elongated funnel is only possible if $\mathscr{F} \gg 1$. Otherwise, the funnel depth would be limited by capillary forces producing a smooth shallow depression. We estimated $h_c \approx 3$ mm from the measurement of the metal puddle thickness over a non-wetted surface. The value of the criterion $\mathscr{F}$ was $\sim$3.5 in figure 4. For $\mathscr{F} < 1$ the depth of the depression was always smaller than its diameter. For $\mathscr{F} > 5$ the funnel produced bubbles that appeared on the surface after the TMF was switched off.

According to our numerical simulations the swirl intensity is almost independent of the RMF for $Ta > Ta_{tr}$. This is consistent with common knowledge about the atmospheric vortices (Rotunno 2013). It also suggests that the funnel depth is determined only by $\mathscr{F}$ for $Ta > Ta_{tr}$. If, however, the vortex is much thinner than the capillary length h_c, then the capillary forces should significantly reduce the funnel depth. We may then require

$$\Gamma_0 \frac{R_0}{h_c} = O(F^{1/2}) \tag{7.7}$$

instead of (7.4) to limit the vortex radius to h_c. This produces a milder scaling $O(F^{-1/4})$, than $O(F^{-5/8})$ (see (7.5)) for the respective magnetic force ratio Ta/F.

8. Summary

A pulse of TMF produces an intense transient tornado-like vortex in a liquid metal cylinder set in rotation by RMF of an appropriate strength. Being strong enough, such a vortex creates a reproducible sharp funnel at the free surface. The funnel is initiated at $t \approx 0.5\tau$, where $\tau \propto F^{-1/2}$ is the initial adjustment time of the TMF-driven spin-up. The funnel is disrupted by violent turbulence which sets in after $t = \tau$. There are two distinct regimes controlled by the strength of the RMF. For a weak RMF the swirl is much weaker than the meridional flow and it increases with Ta while the vortex width stays independent of RMF. The vortex breakdown, if any, is limited to the lower half of the cylinder. For a strong RMF the swirl intensity stays nearly constant $\propto F^{1/2}$ while the vortex diameter increases with Ta and the vortex breakdown fills its inner core over the whole height. The transition between those regimes is similar to that in a developed flow with the exception of the critical force ratio Ta_{tr}/F, which decreases with F and has a much lower value. This difference is explained by a much weaker turbulence during the spin-up which also enables a much higher degree of swirl concentration.

Acknowledgement

Financial support of this research by the German Helmholtz Association in the frame of the Helmholtz-Alliance LIMTECH is gratefully acknowledged.

Supplementary movies

Supplementary movies are available at http://dx.doi.org/10.1017/jfm.2013.552.

REFERENCES

Andersen, A., Bohr, T., Stenum, B., Juul Rasmussen, J. & Lautrup, B. 2006 The bathtub vortex in a rotating container. *J. Fluid Mech.* **556**, 121–146.

Canuto, C., Hussaini, M. Y., Quarteroni, A. & Zhang, T. A. 1988 *Spectral Methods in Fluid Dynamics*. Springer.

https://doi.org/10.1017/jfm.2013.552 Published online by Cambridge University Press

CHURCH, C. R., SNOW, J. T. & AGEE, E. M. 1977 Tornado vortex simulation at Purdue University. *Bull. Am. Meteorol. Soc.* **58**, 900–909.

CHURCH, C. R., SNOW, J. T., BAKER, G. L. & AGEE, E. M. 1979 Characteristics of tornado-like vortices as a function of swirl ratio: a laboratory investigation. *J. Atmos. Sci.* **36**, 1755–1776.

CRAMER, A., PAL, J. & & GERBETH, G. 2007 Experimental investigation of a flow driven by a combination of a rotating and a travelling magnetic field. *Phys. Fluids* **19** (11), 118109.

DAVIDSON, P. A. 1992 Swirling flow in an axisymmetric cavity of arbitrary profile, driven by a rotating magnetic field. *J. Fluid Mech.* **254**, 669–699.

EMANUEL, K. A. 1991 The theory of hurricanes. *Annu. Rev. Fluid Mech.* **23** (1), 179–196.

EMANUEL, K. 2003 Tropical cyclones. *Annu. Rev. Earth Planet. Sci.* **31** (1), 75–104.

FIEDLER, B. H. 1995 On modelling tornadoes in isolation from the parent storm. *Atmos.-Ocean* **33** (3), 501–512.

FIEDLER, B. H. 1998 Wind-speed limits in numerically simulated tornadoes with suction vortices. *Q. J. R. Meteorol. Soc.* **124**, 2377–2392.

FIEDLER, B. 2009 Suction vortices and spiral breakdown in numerical simulations of tornado-like vortices. *Atmos. Sci. Lett.* **10** (2), 109–114.

GRANTS, I. & GERBETH, G. 2001 Stability of axially symmetric flow driven by a rotating magnetic field in a cylindrical cavity. *J. Fluid Mech.* **431**, 407–426.

GRANTS, I. & GERBETH, G. 2004 Stability of melt flow due to a travelling magnetic field in a closed ampoule. *J. Cryst. Growth* **269** (2), 630–638.

GRANTS, I., ZHANG, C., ECKERT, S. & GERBETH, G. 2008 Experimental observation of swirl accumulation in a magnetically driven flow. *J. Fluid Mech.* **616**, 135–152.

GRANTS, I., ZHANG, C., ECKERT, S. & GERBETH, G. 2009 Liquid metal tornado. In *Proceedings of 6th International Conference on Electromagnetic Processing of Materials* (ed. G. Gerbeth & Y. Fautrelle), pp. 102–105. Helmholtz-Zentrum Dresden-Rossendorf.

HALÁSZ, G., GYÜRE, B., JÁNOSI, I. M., SZABÓ, K. G. & TÉL, T. 2007 Vortex flow generated by a magnetic stirrer. *Am. J. Phys.* **75**, 1092–1098.

KLEMP, J. B. 1987 Dynamics of tornadic thunderstorms. *Annu. Rev. Fluid Mech.* **19** (1), 369–402.

LANTZSCH, R., GALINDO, V., GRANTS, I., ZHANG, C., PÄTZOLD, O., GERBETH, G. & STELTER, M. 2007 Experimental and numerical results on the fluid flow driven by a travelling magnetic field. *J. Cryst. Growth* **305**, 249–256.

LEWELLEN, D. C., LEWELLEN, W. S. & XIA, J. 2000 The influence of a local swirl ratio on tornado intensification near the surface. *J. Atmos. Sci.* **57** (4), 527–544.

LEWELLEN, W. S., LEWELLEN, D. C. & SYKES, R. I. 1997 Large-eddy simulation of a tornado's interaction with the surface. *J. Atmos. Sci.* **54** (5), 581–605.

MARKOWSKI, P., RICHARDSON, Y., RASMUSSEN, E., STRAKA, J., DAVIES-JONES, R. & TRAPP, R. J. 2008 Vortex lines within low-level mesocyclones obtained from pseudo-dual-Doppler radar observations. *Mon. Weath. Rev.* **136** (9), 3513–3535.

NIKRITYUK, P. A., UNGARISH, M., ECKERT, K. & GRUNDMANN, R. 2005 Spin-up of a liquid metal flow driven by a rotating magnetic field in a finite cylinder: a numerical and an analytical study. *Phys. Fluids* **17**, 067101.

NOLAN, D. S. 2005 A new scaling for tornado-like vortices. *J. Atmos. Sci.* **62** (7), 2639–2645.

PROCHAZKA, A. & PULLIN, D. I. 1995 On the two-dimensional stability of the axisymmetric Burgers vortex. *Phys. Fluids* **7**, 1788–1790.

RÄBIGER, D., ECKERT, S. & GERBETH, G. 2010 Measurements of an unsteady liquid metal flow during spin-up driven by a rotating magnetic field. *Exp. Fluids* **48** (2), 233–244.

ROBINSON, T. & LARSSON, K. 1973 An experimental investigation of a magnetically driven rotating liquid-metal flow. *J. Fluid Mech.* **60**, 641–664.

ROTUNNO, R. 2013 The fluid dynamics of tornadoes. *Annu. Rev. Fluid Mech.* **45** (1), 59–84.

TACKE, K. H. & SCHWERDTFEGER, K. 1979 Rührgeschwindigkeit in Rundstrangguss bei Rührung mit elektromagnetischen Drehfeldern. *Stahl Eisen.* **99** (1), 7–12.

WARD, N. B 1972 The exploration of certain features of tornado dynamics using a laboratory model. *J. Atmos. Sci.* **29** (6), 1194–1204.

YIH, C. S. 2007 Tornado-like flows. *Phys. Fluids* **19** (7), 076601.

https://doi.org/10.1017/jfm.2013.552 Published online by Cambridge University Press